Journal of Non-Newtonian Fluid Mechanics 195 (2013) 19–31

Contents lists available at SciVerse ScienceDirect

Journal of Non-Newtonian Fluid Mechanics

journal homepage: http://www.elsevier.com/locate/jnnfm

Solution of the square lid-driven cavity flow of a Bingham plastic using the finite volume method

Alexandros Syrakos [a], Georgios C. Georgiou [b,a,*], Andreas N. Alexandrou [c]

[a] Oceanography Centre, University of Cyprus, PO Box 20537, 1678 Nicosia, Cyprus
[b] Department of Mathematics and Statistics, University of Cyprus, PO Box 20537, 1678 Nicosia, Cyprus
[c] Department of Mechanical and Manufacturing Engineering, University of Cyprus, PO Box 20537, 1678 Nicosia, Cyprus

ARTICLE INFO

Article history:
Received 13 October 2012
Received in revised form 3 December 2012
Accepted 7 December 2012
Available online 11 January 2013

Keywords:
Bingham plastic
Papanastasiou regularisation
Lid-driven cavity
Finite volume method
SIMPLE
Multigrid

ABSTRACT

We investigate the performance of the finite volume method in solving viscoplastic flows. The creeping square lid-driven cavity flow of a Bingham plastic is chosen as the test case and the constitutive equation is regularised as proposed by Papanastasiou [J. Rheol. 31 (1987) 385–404]. It is shown that the convergence rate of the standard SIMPLE pressure-correction algorithm, which is used to solve the algebraic equation system that is produced by the finite volume discretisation, severely deteriorates as the Bingham number increases, with a corresponding increase in the non-linearity of the equations. It is shown that using the SIMPLE algorithm in a multigrid context dramatically improves convergence, although the multigrid convergence rates are much worse than for Newtonian flows. The numerical results obtained for Bingham numbers as high as 1000 compare favourably with reported results of other methods.

1. Introduction

Viscoplastic flows constitute an important branch of non-Newtonian fluid mechanics, as many materials of industrial, geophysical, and biological importance are known to exhibit yield stress. In general, yield-stress fluids are suspensions of particles or macromolecules, such as pastes, gels, foams, drilling fluids, food products, and nanocomposites. A comprehensive review of viscoplasticity has been carried out by Barnes [1]. Such materials behave as (elastic or inelastic) solids, below a certain critical shear stress level, i.e. the yield stress, and as liquids otherwise. The flow field is thus divided into unyielded (rigid) and yielded (fluid) regions.

The simplest constitutive equation describing viscoplasticity is that proposed by Bingham [2]:

$$\begin{cases} \dot{\boldsymbol{\gamma}} = \mathbf{0}, & \tau \leqslant \tau_y \\ \boldsymbol{\tau} = (\frac{\tau_y}{\dot{\gamma}} + \mu)\dot{\boldsymbol{\gamma}}, & \tau > \tau_y \end{cases} \tag{1}$$

where τ_y is the yield stress, μ is the plastic viscosity, $\boldsymbol{\tau}$ is the stress tensor, $\dot{\boldsymbol{\gamma}}$ is the rate of strain tensor,

$$\dot{\boldsymbol{\gamma}} \equiv \nabla\mathbf{u} + (\nabla\mathbf{u})^{\mathrm{T}} \tag{2}$$

$\mathbf{u}$ is the velocity vector, and the superscript T denotes the transpose of the velocity-gradient tensor $\nabla\mathbf{u}$. The symbols τ and $\dot{\gamma}$ denote the magnitudes of the stress and rate-of-strain tensors, respectively:

$$\tau \equiv \left[\frac{1}{2}\boldsymbol{\tau} : \boldsymbol{\tau}\right]^{\frac{1}{2}}, \quad \dot{\gamma} \equiv \left[\frac{1}{2}\dot{\boldsymbol{\gamma}} : \dot{\boldsymbol{\gamma}}\right]^{\frac{1}{2}} \tag{3}$$

Another two-parameter viscoplastic equation is the Casson model, which is mostly used in hemodynamics. The Herschel–Bulkley model is the generalisation of the Bingham-plastic equation, which involves a power-law exponent allowing shear-thinning or shear thickening.

Simulating viscoplastic flows poses extra-ordinary difficulties due to the discontinuity of the constitutive equations. In most cases, it is necessary to determine the location and the shape of the yield surface at which the flow switches from one branch of the constitutive equation to the other, e.g. from solid to liquid behaviour. Mathematically, the yield surface is the locus of points where $\tau = \tau_y$. A common approach to overcoming this burden is to regularise the constitutive equation, i.e. to describe the two branches of (1) by one smooth equation using a stress-growth parameter. The most popular regularisation is that proposed by Papanastasiou [3]:

$$\boldsymbol{\tau} = \left[\frac{\tau_y}{\dot{\gamma}}\{1 - \exp(-m\dot{\gamma})\} + \mu\right]\dot{\boldsymbol{\gamma}} \tag{4}$$

* Corresponding author. Tel.: +357 22892612; fax: +357 22895352.
E-mail addresses: syrakos.alexandros@ucy.ac.cy (A. Syrakos), georgios@ucy.ac.cy (G.C. Georgiou), andalexa@ucy.ac.cy (A.N. Alexandrou).

0377-0257/$ - see front matter © 2013 Elsevier B.V. All rights reserved.
http://dx.doi.org/10.1016/j.jnnfm.2012.12.008

where m denotes the stress growth parameter, which needs to be "sufficiently" large. Frigaard and Nouar [4] reviewed systematically the convergence of the Papanastasiou and other regularized models including the bi-viscosity model [5].

Another approach in solving viscoplastic flows is based on the use of variational inequalities, that is rate-of-strain minimisation or stress maximisation, which form the basis of the Augmented Lagrangian Method [6,7]. Dean et al. [8] reviewed and compared numerical methods based on the variational inequality approach.

In this paper, we adopt the regularisation approach and investigate the performance of the finite volume/multigrid method in solving Bingham plastic flows. The finite volume method (FVM) is a popular method for solving fluid flows, employed by many general-purpose CFD solvers. One of the attractive features of the method is that it can be applied to a variety of physical problems with relative ease. However, there are a limited number of published results on the use of the finite-volume method to solve Bingham flow problems. Neofytou [9] used a FVM in conjunction with the SIMPLE algebraic solver [10] to simulate the lid-driven cavity flow of various non-Newtonian fluids, including a Papanastasiou-regularised Bingham plastic at quite low Bingham numbers (0.01–1). Turan and co-workers [11,12] also used a commercial FVM/SIMPLE code employing the bi-viscosity model in order to simulate natural convection of a Bingham plastic in a square cavity. The FVM was also used to solve flows of a Casson fluid through a stenosis [13] and through a sudden expansion [14], at rather low yield-stress values. Also, de Souza Mendes et al. [15] and Naccache and Barbosa [16] used the FVM in order to simulate viscoplastic flow through an expansion followed by a contraction.

A benchmark problem for testing numerical methods for both Newtonian and non-Newtonian flows is the lid-driven cavity flow problem. For laminar Newtonian flow, the reader is referred to the works of Botella and Peyret [17], Syrakos and Goulas [18], Bruneau and Saad [19], and the references therein. The lid-driven cavity flow has also been used as a test case for Bingham flows by Sanchez [20], Mitsoulis and Zisis [21], Vola et al. [22], Elias et al. [23], Yu and Wachs [24], Olshanskii [25], Zhang [26], and dos Santos et al. [27], who used solution methods other than the FVM, mostly the Finite Element method. To the authors' knowledge, only Neofytou [9] used the FVM in order to solve the driven cavity flow of a Bingham plastic or any other viscoplastic fluid, albeit for very small Bingham numbers ($\leqslant 1$). Although some of the aforementioned published works contain results for non-zero Reynolds numbers, in most cases the results concern creeping flows ($Re = 0$).

The objective of the present work is to apply the FVM along with a multigrid method in order to improve the convergence of the SIMPLE solver when solving the lid-driven cavity Bingham flow for a broad range of Bingham numbers. Multigrid methods use a hierarchy of grids of progressive fineness. By applying the algebraic solver on each of these grids, all wavelengths of the algebraic error are reduced with equal efficiency. Multigrid methods were originally proposed by Fedorenko [28] and later developed by Brandt [29]. In the context of the FVM, they were first used in the late 1980s [30,31]. Since then, they have been employed in numerous studies involving the FVM, many of which used the lid-driven cavity flow of a Newtonian fluid as a test problem; see Syrakos and Goulas [18] and references therein. These Newtonian studies have shown that using multigrid algorithms can result in very significant performance gains. To our knowledge, the finite volume/multigrid method has not been tested in the case of Bingham flow.

The rest of the paper is organised as follows. In Section 2, the integral forms of the governing equations are presented and dedimensionalized. In Section 3, the numerical method, that is the discretisation of the governing equations and the solution of the resulting algebraic system, is discussed. The numerical results are presented in Section 4. These compare well with the results of Mitsoulis and Zisis [21] and Yu and Wachs [24]. The convergence of the algebraic solver has also been studied and possible ways for its acceleration have been investigated. Finally, Section 5 contains our concluding remarks.

2. Governing equations

We consider the steady-state, two-dimensional flow in a square cavity of side L, the top boundary (lid) of which moves towards the right with a uniform horizontal velocity U, while the remaining sides are fixed. We work in Cartesian coordinates (x, y), centred at the lower-left corner of the cavity and denote the unit vectors in the x and y directions by $\mathbf{i}$ and $\mathbf{j}$, respectively. Let also ρ and $\eta = \eta(\dot\gamma)$ denote the density and the viscosity of any generalised-Newtonian fluid. By means of the Gauss theorem, the integral forms of the continuity and the x- and y- components of the momentum equations over a control volume P are as follows:

$$\int_{S_P} \rho \mathbf{u} \cdot d\mathbf{S} = 0 \tag{5}$$

$$\int_{S_P} \rho u \mathbf{u} \cdot d\mathbf{S} = \int_{S_P} \eta \left(\nabla u + \frac{\partial \mathbf{u}}{\partial x} \right) \cdot d\mathbf{S} - \int_{S_P} p\mathbf{i} \cdot d\mathbf{S} \tag{6}$$

$$\int_{S_P} \rho v \mathbf{u} \cdot d\mathbf{S} = \int_{S_P} \eta \left(\nabla v + \frac{\partial \mathbf{u}}{\partial y} \right) \cdot d\mathbf{S} - \int_{S_P} p\mathbf{j} \cdot d\mathbf{S} \tag{7}$$

where S_P is the boundary surface of the control volume, $d\mathbf{S}$ is an infinitesimal element of this surface oriented so that the normal vector points out of P, $\mathbf{u} = u\mathbf{i} + v\mathbf{j}$ is the velocity vector, and p is the pressure. In the case of the Papanastasiou model (4), the viscosity is given by

$$\eta = \frac{\tau_y}{\dot\gamma} \{1 - \exp(-m\dot\gamma)\} + \mu \tag{8}$$

The advantage of the Papanastasiou regularisation is that expression (8) is used over the entire flow domain, i.e. over both yielded and unyielded regions. At high strain rates the viscosity tends towards μ if the growth parameter m is large enough. In the unyielded regions the viscosity obtains high values which result in very small values of $\dot\gamma$ and thus solid body motion is approximated. When $\dot\gamma$ tends to zero, then the viscosity (8) tends not to infinity but to the finite value $m\tau_y + \mu$. Some authors [32,33] suggested that lower values of m can be used at higher yield stress values and vice versa.

To dedimensionalise the governing Eqs. (5)–(7), we scale lengths by the cavity side L, the velocity components by U, and the pressure and stress by $\mu U/L$, and use stars to denote the dimensionless variables. Taking into account that ρ is constant, the dimensionless equations are as follows:

$$\int_{S_P} \mathbf{u}^* \cdot d\mathbf{S}^* = 0 \tag{9}$$

$$Re \int_{S_P^*} u^* \mathbf{u}^* \cdot d\mathbf{S}^* = \int_{S_P^*} \eta^* \left(\nabla^* u^* + \frac{\partial \mathbf{u}^*}{\partial x^*} \right) \cdot d\mathbf{S}^* - \int_{S_P^*} p^* \mathbf{i} \cdot d\mathbf{S}^* \tag{10}$$

$$Re \int_{S_P^*} v^* \mathbf{u}^* \cdot d\mathbf{S}^* = \int_{S_P^*} \eta^* \left(\nabla^* v^* + \frac{\partial \mathbf{u}^*}{\partial y^*} \right) \cdot d\mathbf{S}^* - \int_{S_P^*} p^* \mathbf{j} \cdot d\mathbf{S}^* \tag{11}$$

$$\eta^* = \frac{Bn}{\dot\gamma^*} \{1 - \exp(-M\dot\gamma^*)\} + 1 \tag{12}$$

where

$$Re \equiv \frac{\rho U L}{\mu} \tag{13}$$

is the Reynolds number,

$$Bn \equiv \frac{\tau_y L}{\mu U} \tag{14}$$

is the Bingham number, and

$$M \equiv \frac{mU}{L} \tag{15}$$

is the stress-growth number.

For the sake of simplicity, the stars denoting the dimensionless variables are dropped hereafter.

3. Numerical method

3.1. Discretisation of the equations

The domain is split into a number of control volumes (CVs) using a Cartesian grid of equally spaced horizontal and vertical grid lines. For each control volume, the continuity and momentum equations are approximated using algebraic expressions involving the values of the unknowns u, v, p at the centre of that CV and at the centres of neighbouring CVs [34]. The computer code which was used for the present study has the ability to use curvilinear grids composed of quadrilateral CVs – see [35,18] for details – but in the present section only the simpler form that these discretisation schemes acquire when the grid is Cartesian will be presented. Although the present work concerns only creeping flow, the treatment of the convection terms of the momentum equations is also described for completeness.

For each CV, the surface flux integrals are calculated separately on each face. Fig. 1 shows a control volume P and its neighbours, S, E, N and W. The letters P, S, E, N and W will also denote the position vectors of the centres of the respective CVs. First, the flow variables and their normal derivatives are calculated at the centre of each face using central differences, e.g. for face e:

$$u_e = \frac{u_E + u_P}{2} \tag{16}$$

$$\left.\frac{\partial u}{\partial x}\right|_e = \frac{u_E - u_P}{\Delta x} \tag{17}$$

The flux integrals are then approximated using the midpoint rule, e.g. for the x-momentum equation:

$$\int_e u\mathbf{u}\cdot d\mathbf{S} \approx F_e u_e \tag{18}$$

$$\int_e \eta\nabla u\cdot d\mathbf{S} \approx \eta_e \left.\frac{\partial u}{\partial x}\right|_e \Delta y \tag{19}$$

$$\int_e p\mathbf{i}\cdot d\mathbf{S} \approx p_e \Delta y \tag{20}$$

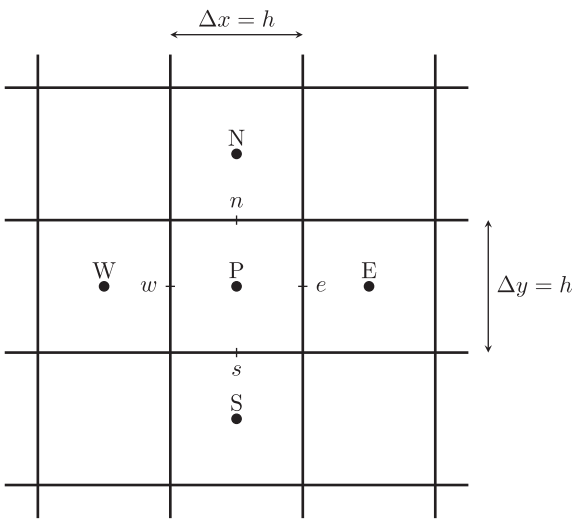

Fig. 1. A control volume P and its neighbours.

Eqs. (18) and (19) do not describe the approximation scheme sufficiently, and some definitions are still missing: F_e denotes the mass flux through face e and will be defined shortly; the term (19) is only part of the total viscous flux; and the term η_e requires that the viscosity has already been calculated somehow at CV centres. To define these terms we first approximate the gradient operator at CV centres (Eq. (17) only approximates the normal component at face centres). At the centre of control volume P the following approximation is used:

$$\left.\frac{\partial u}{\partial x}\right|_P = \frac{u_E - u_W}{2\Delta x}, \quad \left.\frac{\partial u}{\partial y}\right|_P = \frac{u_N - u_S}{2\Delta y} \tag{21}$$

If P is a boundary CV, and the domain boundary coincides with face w, then the horizontal component of the gradient is calculated as follows:

$$\left.\frac{\partial u}{\partial x}\right|_P = \frac{u_E + u_P - 2u_w}{2\Delta x} \tag{22}$$

where u_w is the boundary value of u, specified by the Dirichlet boundary condition.

Now, the viscosity is calculated at CV centres from Eq. (12), where $\dot\gamma$ is calculated from (3), using the velocity gradients at CV centres (21):

$$\dot\gamma_P = \left[2\left(\left.\frac{\partial u}{\partial x}\right|_P\right)^2 + 2\left(\left.\frac{\partial v}{\partial y}\right|_P\right)^2 + \left(\left.\frac{\partial u}{\partial y}\right|_P + \left.\frac{\partial v}{\partial x}\right|_P\right)^2\right]^{\frac{1}{2}} \tag{23}$$

Thus η_e in (19) is calculated from η_P and η_E using linear interpolation (16). Since the viscosity is only needed at face centres, an alternative would be to calculate it there directly. This would require the velocity gradients at the face centres, the normal component of which is readily available from (17). But the tangential component is not, and would require interpolation of velocity components at face vertices. So, this alternative would not be less complex than the approach presently adopted.

For the same reason, the remaining part of the viscous fluxes is also calculated by interpolating the velocity gradients at face centres from the CV centres. For example, for faces e and n we have, respectively:

$$\int_e \eta\frac{\partial \mathbf{u}}{\partial x}\cdot d\mathbf{S} \approx \eta_e\left(\frac{\partial u}{\partial x}\right)_e \Delta y, \quad \int_n \eta\frac{\partial \mathbf{u}}{\partial x}\cdot d\mathbf{S} \approx \eta_n\left(\frac{\partial v}{\partial x}\right)_n \Delta x \tag{24}$$

Here the derivatives $(\partial u/\partial x)_e$ and $(\partial v/\partial x)_e$ are not the same as in Eq. (17), but are interpolated from the derivatives (21) at face centres according to (16). This approach is convenient in the case of curvilinear grids, which is why it is adopted by the code we used for the present study.

This leaves only the mass fluxes to be defined. These are discretised using the central difference scheme (16), but with the addition of an artificial pressure term whose role is to not allow the appearance of spurious pressure oscillations in the discrete solution. The mass flux through face e, in non-dimensional form, is discretised as:

$$\begin{aligned} F_e &= \int_e \mathbf{u}\cdot d\mathbf{S} \\ &\approx u_e\Delta y + \frac{(\Delta y)^2}{a_e}\left[(p_P - p_E) - \frac{1}{2}\left(\left.\frac{\partial p}{\partial x}\right|_P + \left.\frac{\partial p}{\partial x}\right|_E\right)(x_P - x_E)\right] \end{aligned} \tag{25}$$

where

$$a_e = Re(|u_e|\Delta y + |v_e|\Delta x) + 2\eta_e\left(\frac{\Delta y}{\Delta x} + \frac{\Delta x}{\Delta y}\right) \tag{26}$$

Without this treatment, artificial pressure oscillations do appear when both velocity and pressure are stored at the CV centres, as in the present scheme. This technique is known as *momentum*

interpolation and was first suggested by Rhie and Chow [36]. The above variant, proposed in [35], has the advantage that it is decoupled from the SIMPLE solution algorithm. The resulting equations simplify further in case of a uniform grid, $\Delta x = \Delta y = h$, but for completeness the more general forms are included here. The artificial pressure term is very small, of order $O(h^5)$, and has a very small impact on the accuracy of the discretisation of the mass flux.

The test cases examined in this work involve only no-slip solid wall boundaries, with Dirichlet boundary conditions. The discretisation there is as follows: The pressure is linearly extrapolated from the interior. The product $\nabla u \cdot d\mathbf{S}$ of the main viscous terms (19) is calculated as a one-sided difference, i.e. if e is a boundary face then $\nabla u \cdot d\mathbf{S}$ is approximated as $\Delta y \cdot (u(e) - u_P)/(\Delta x/2)$ where $u(e)$ is the exact value of u at the centre of face e, as defined by the Dirichlet boundary condition. Finally, in the secondary viscous terms (24) both the derivative and the viscosity at the boundary face centre are taken as equal to their values at the adjacent CV centre.

By substituting all terms in the continuity and momentum equations of each CV by their discrete counterparts, a non-linear algebraic system is obtained, with four equations (x, y-momentum, continuity and constitutive equation) and four unknowns (u, v, p, η) per CV. The overall discretisation scheme is of second order accuracy, meaning that the discretisation error should decrease as $O(h^2)$. Solution of this algebraic system gives the values of the unknowns, up to the discretisation error. The solver used to solve this system is described next.

3.2. Solution of the algebraic system

The popular SIMPLE algorithm [10] was chosen as the non-linear solver. It is a widely used algorithm and so it will not be fully described here – the interested reader is referred to [37] or [34]. In brief, SIMPLE is an iterative algorithm which constructs and solves a number of linear systems within each iteration. These linear systems come from breaking up and linearising the set of discretised equations: The systems of equations for the momentum components are converted into linear systems for the corresponding velocity components by evaluating some of the terms (including the viscosity (12)) using the velocity and pressure values obtained from the previous SIMPLE iteration; and the continuity equations system is used to construct an approximate "pressure correction" linear system, which attempts to improve the current pressure estimate so as to force the velocity field to be more continuity-conservant. A SIMPLE iteration (outer iteration) consists of the successive solution of the linear systems of the velocity components and of pressure correction. Only a few iterations (inner iterations) of a linear solver are applied to each linear system, since the matrices of coefficients will change in the next outer SIMPLE iteration. In this work we used GMRES as the linear solver for the velocity systems, and conjugate gradients (CG) for the pressure correction system, preconditioned by incomplete factorisations with zero fill-in – see [38] for detailed descriptions. To achieve convergence, underrelaxation factors a_u, $a_p < 1$ are applied to the velocity and pressure correction systems respectively [34]. SIMPLE iterations are repeated until the residuals of all the original non-linear algebraic equations drop below a selected threshold.

The only modification needed so that SIMPLE can be used for Bingham or other generalised-Newtonian flows is that, at the start of every SIMPLE iteration, the viscosity must be updated at each CV according to (12), using the current estimate of the velocity field to calculate $\dot{\gamma}$.

The SIMPLE algorithm converges rather slowly, so it was decided to implement it in a multigrid context to accelerate its convergence. Many algebraic solvers are able to quickly reduce the short wavelengths of the error but are quite slow in reducing the longer wavelengths. SIMPLE is such a solver [39], not only because the linear solvers used for the inner iterations may themselves have this property, but also because of local assumptions made in the linearisation of the non-linear terms and in the construction of the pressure correction equation, which relate a CV to its direct neighbours. In such a case, after a few iterations have been performed and the short wavelengths of the error have been reduced, it is beneficial to move the solution procedure to a coarser grid, where the direct neighbours of a CV are farther away and so the long wavelengths of the error appear shorter and can be reduced more efficiently by the same algebraic solver. By using a cascade of progressively coarser grids, all wavelengths of the error can be reduced with equal efficiency [29].

The solution procedure is transferred between grids as follows. Let the system of all algebraic equations be written as:

$$N_h(x_h) = b_h \tag{27}$$

where now the vector x_h stores all the unknowns (velocity components, pressure, and viscosity) at all CV centres of the grid whose spacing is h. After a few SIMPLE iterations an approximate solution x_h^* is obtained which satisfies the above equation up to a residual r_h:

$$N_h(x_h^*) = b_h - r_h = N_h(x_h) - r_h \Rightarrow N_h(x_h) = N_h(x_h^*) + r_h \tag{28}$$

The algebraic system (28) can be approximated on a coarser grid of spacing $2h$ (grid $2h$ hereafter), obtained by removing every second grid line of grid h, as follows:

$$N_{2h}(x_{2h}) = N_{2h}\left(I_h^{2h} x_h^*\right) + \widehat{I}_h^{2h} r_h \tag{29}$$

The operator N_{2h} is constructed on grid $2h$ using the same discretisation schemes as N_h on grid h, with $2\Delta x$ and $2\Delta y$ used instead of Δx and Δy. The *restriction* operator I_h^{2h} transfers the variables from grid h to grid $2h$. The notation comes from the identity matrix I, since the variables are not transformed but rather transferred from one grid to another. In the present study this restriction operator sets the value of a variable at the centre of a control volume P of grid $2h$ equal to the average of the values of that variable over the 4 CVs of grid h that overlap with P, which will hereafter be called the *children* of P. The (possibly different) operator $\widehat{I}_h^{2h}$ is used for transferring the residuals to grid $2h$. In the present study the residuals at a control volume P of grid $2h$ are set equal to the sum of the

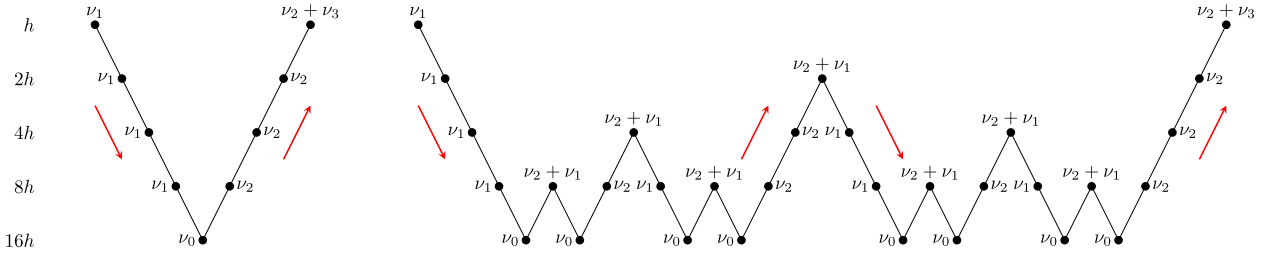

Fig. 2. Multigrid cycles: V(ν_1, ν_2) – ν_3 (left) and W(ν_1, ν_2) – ν_3 (right) cycles, using 5 grid levels.

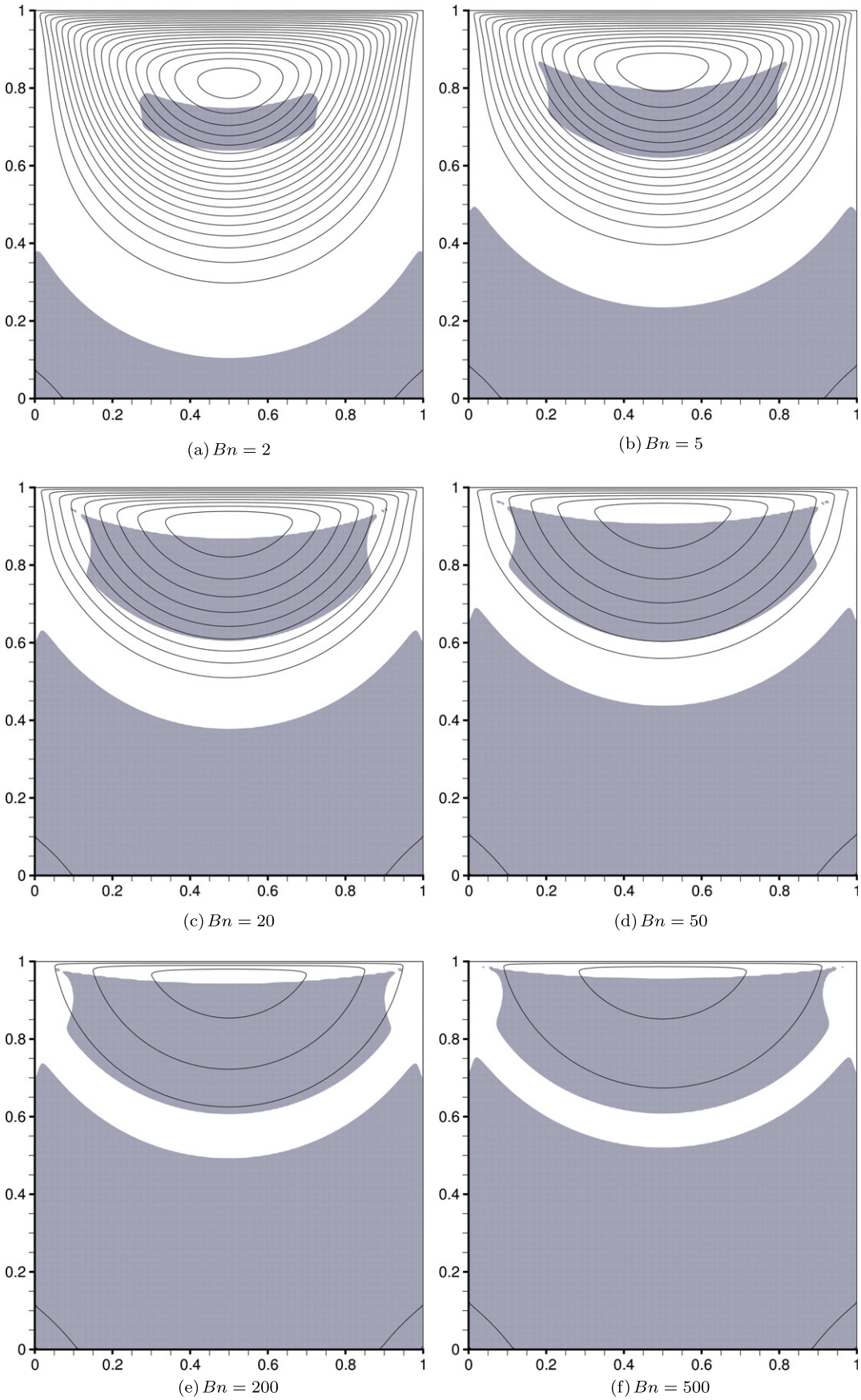

Fig. 3. Streamlines plotted at intervals of 0.004 starting from zero. Unyielded areas ($\tau < Bn$) are shown shaded.

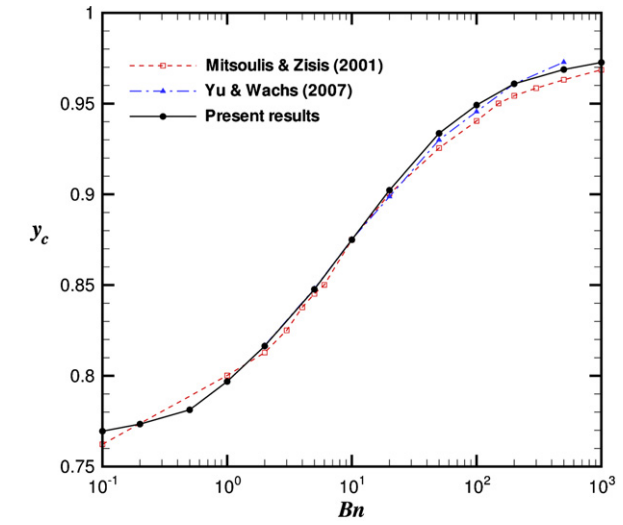

(a) Vortex centre

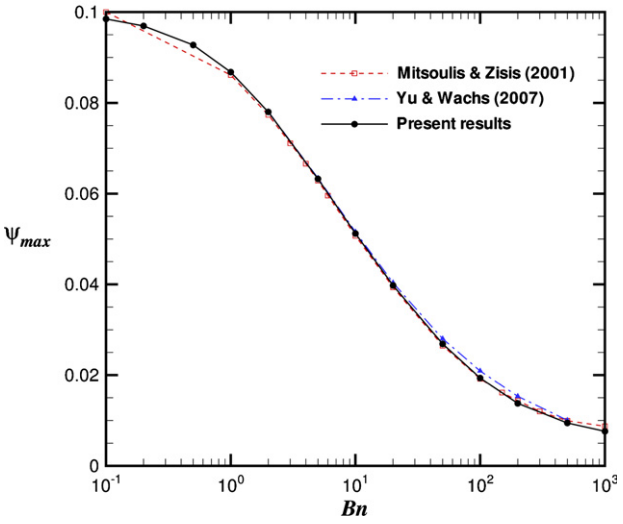

(b) Vortex strength

Fig. 4. The y coordinate of the centre of the vortex, and vortex strength as a function of the Bingham number.

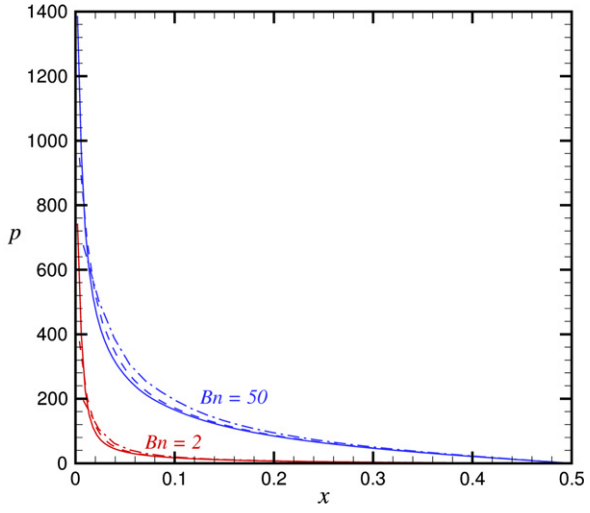

(a) p at the lid

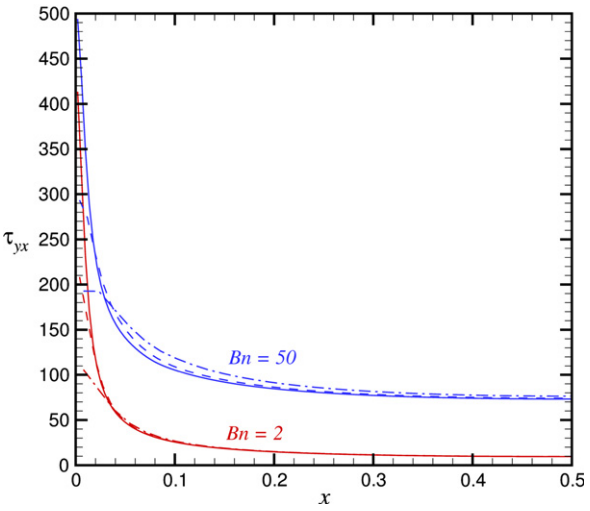

(b) τ_{yx} at the lid

Fig. 5. Pressure and shear stress at the left half of the lid for $Bn = 2$ and 50. Results are shown for grids 64×64 (chained lines), 128×128 (dashed lines), and 256×256 (solid lines).

residuals of all its children. Since the residuals are essentially flux imbalances, this means that the flux imbalance of P is set equal to the sum of the imbalances of its children.

The right hand side of (29) is known, so the system can be solved to obtain x_{2h}. Then, the *correction* $x_{2h} - I_h^{2h} x_h^*$ is transferred back to grid h, to obtain a better estimate x_h^{new} of the exact solution x_h, and SIMPLE iterations can resume on grid h:

$$x_h^{new} = x_h^* + I_{2h}^h \left(x_{2h} - I_h^{2h} x_h^* \right) \tag{30}$$

The *prolongation* operator I_{2h}^h transfers the correction from grid $2h$ to grid h; in the present study linear interpolation is used. It is straightforward to see that if in (28) the exact solution has already been obtained $(x_h^* = x_h)$ then the residuals will be zero and therefore so will be the last term of (29). Then the solution of (29) will be $x_{2h} = I_h^{2h} x_h^*$ (it is important that $I_h^{2h} x_h^*$ be used as the initial guess when solving (29)), and therefore the correction $x_{2h} - I_h^{2h} x_h^*$ will be zero. So, (30) will leave the solution unaltered: $x_h^{new} = x_h^* = x_h$.

The coarse grid problem (29) can be solved using an even coarser grid $4h$ and so on. This whole process of going down from grid h to some coarsest grid and then back again up to grid h constitutes a *multigrid cycle*. In general, a number of multigrid cycles will be required to reduce the residuals by a given amount. Different kinds of cycles have been suggested and used. The most popular are the $V(\nu_1, \nu_2)$ and $W(\nu_1, \nu_2)$ cycles. In $V(\nu_1, \nu_2)$ cycles, after performing ν_1 iterations on the fine grid h, the coarse grid system (29) is solved using one multigrid cycle, and then the coarse grid correction is transferred back to grid h according to (30), where another ν_2 iterations are performed. The difference between the W and V cycles is that in W cycles the coarse grid problems such as (29) are solved using two rather than one cycle. In the present work we have observed that it is sometimes useful to perform ν_3 extra SIMPLE iterations on the finest grid h only, between cycles. Such cycles will be denoted $V(\nu_1, \nu_2) - \nu_3$ or $W(\nu_1, \nu_2) - \nu_3$ respectively. These cycles are shown schematically in Fig. 2. The costs of a $V(\nu_1, \nu_2) - \nu_3$ and a $W(\nu_1, \nu_2) - \nu_3$ cycle are approximately equal to $\left[\frac{4}{3}(\nu_1 + \nu_2) + \nu_3\right]$ and $[2(\nu_1 + \nu_2) + \nu_3]$ times the cost of a single iteration on the finest grid h, respectively.

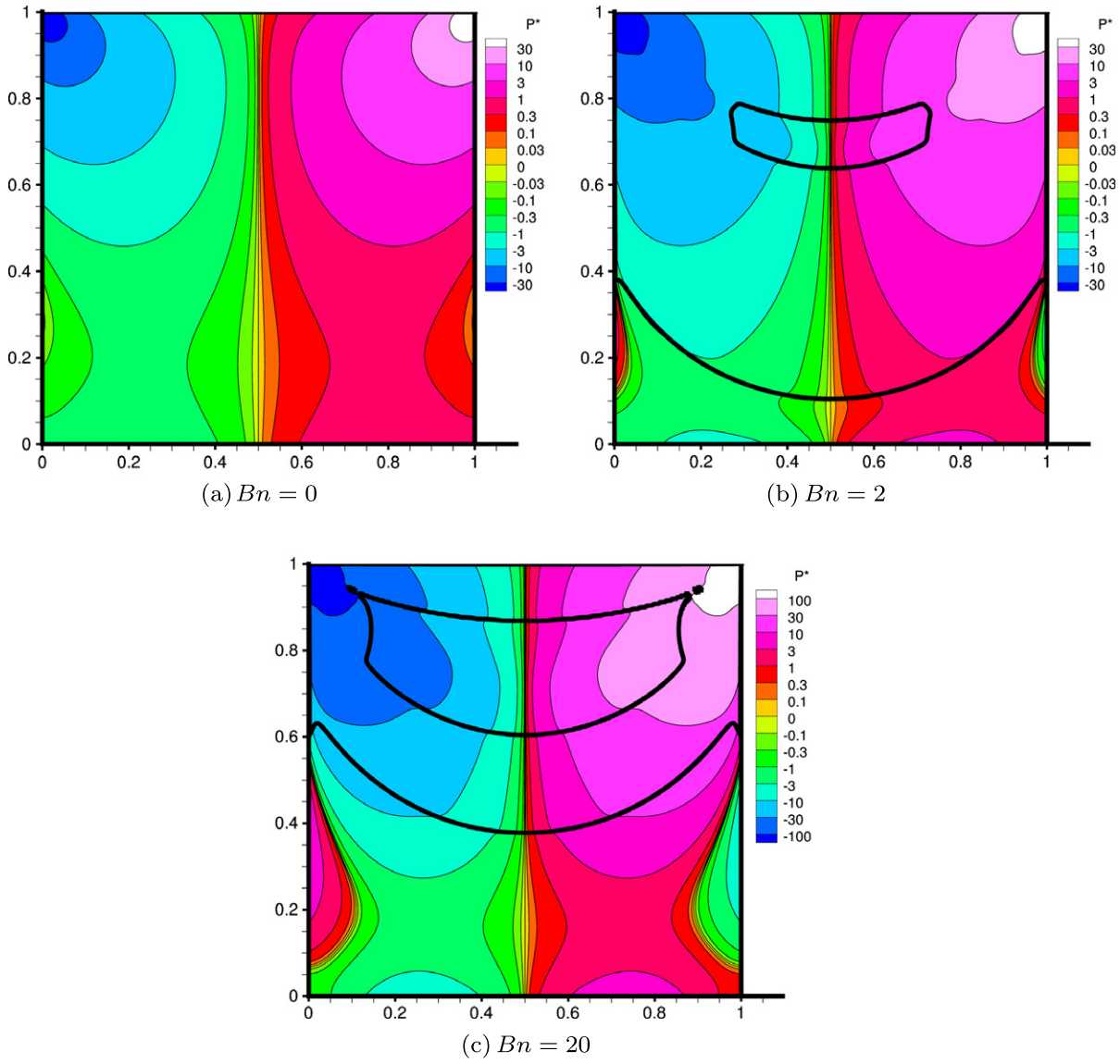

Fig. 6. Pressure contours for various *Bn* numbers. For $Bn \neq 0$ the thick lines outline the unyielded regions. Note that the pressure scale of the $Bn = 20$ case is different.

4. Numerical results

The creeping flow ($Re = 0$) of a Bingham plastic in a square lid-driven cavity has been chosen as the test case for the finite volume method described in the previous section. The computational domain is a square, enclosed by solid boundaries of equal length. The top boundary (lid) moves towards the right with a uniform horizontal velocity, while the rest of the boundaries are still. The problem was solved for a range of Bingham numbers, up to 1000. In all cases an exponent $M = 400$ was used, except for the two highest Bingham numbers tested, $Bn = 500$ and 1000, for which $M = 100$ was used due to convergence difficulties. In order to check grid convergence, the domain was discretised using three uniform Cartesian grids with 64×64, 128×128 and 256×256 CVs. Unless otherwise stated, the results presented below were calculated on the 256×256 grid. The pressure was set to zero at the centre of the domain.

Fig. 3 shows the streamlines calculated for selected Bingham numbers. These are the Bingham numbers chosen also by Mitsoulis and Zisis [21] and Yu and Wachs [24] for their corresponding figures. The "unyielded" regions are also shown. These are defined here as the regions where $\tau < Bn$, where $\tau = \eta\dot{\gamma}$ is calculated from (12) and (23). Of course, they are not actually unyielded, but they approximate the unyielded regions of an ideal Bingham flow. The results generally agree with those presented by other researchers, in [21,24–26]. The agreement is good with the results of Mitsoulis and Zisis [21] in the whole range of Bingham numbers, except that these authors predict yielded regions with more rounded corners than the present results. Also, their yield surfaces are not smooth, but this may be due to the low resolution of the grid that they employed. The results also agree well with those of Yu and Wachs [24] up to a Bingham number of 20, but there are notable differences at higher Bingham numbers-however, Yu and Wachs state that, as far as capturing the yield surface is concerned, their method performs well at low to moderate Bingham numbers but less so at high Bingham numbers. Direct comparison can also be made between the present results and those of Olshanskii [25] for $Bn = 2$ and $Bn = 5$, who used an augmented Lagrangian approach instead of a regularisation method, and the agreement is very good. Zhang [26], who also used an augmented Lagrangian approach, also provides results

for $Bn = 2$, 20, 50 and 200, where the unyielded regions appear somewhat smaller, flatter, and rounded compared to the present results, although qualitatively similar.

The main characteristic of the flow field is the vortex which develops at the upper central region of the cavity, similarly to the Newtonian case. Two distinct unyielded regions can be observed: A larger one at the bottom of the cavity, and a smaller one just below the vortex centre. The flow field is symmetric with respect to the vertical centreline. As the Bn number increases, the unyielded regions expand and the flow circulation becomes weaker and limited to the upper part of the cavity, with the centre of the vortex coming closer to the lid. One can notice in Fig. 3 that a couple of secondary vortices appear at the lower two corners of the cavity, which are completely inside the lower unyielded region. These vortices, which appear to slightly grow in size as Bn increases, are an artifact of the regularisation of the Bingham model by the Papanastasiou approximation. In fact, the velocity is extremely low throughout the lower unyielded region. In reality, since this region is in contact with the rigid walls which are motionless, and a no-slip boundary condition applies, the unyielded material should also be motionless throughout.

The situation is different at the upper unyielded region, where the velocity is non-zero as can be clearly seen from the streamlines' spacing. So, the upper unyielded regions move as solid bodies. In the present case it appears that the material at the upper unyielded region moves as a solid body, and in particular it rotates, with the streamlines forming circular arcs inside it. The fact that the streamlines cross into this region means that the fluid "solidifies" on entry, and becomes fluid again on exit from the region.

The behaviour of the vortex as a function of the Bn number is described in more detail in Fig. 4, where the vertical position and the strength of the vortex are plotted as functions of Bn. The weakening of the circulation as Bn increases is accompanied by an increase in the stress and pressure levels in the cavity, as greater stresses are needed in order to make the material flow. Fig. 4 also serves to validate the results of the present study against those of other researchers. It can be seen that the results are quite close to previously published data of [21] and [24]. The results are closer to those of Mitsoulis and Zisis [21] as far as the vortex strength is concerned, and to the results of Yu and Wachs [24] as far as the vortex position is concerned (possibly because the grid of [21] is coarse).

Fig. 5 shows the pressure and shear stress distributions at the left half of the lid. Increasing the Bingham number from 2 to 50 causes a significant increase in pressure and stress, as discussed previously. Fig. 5 can also be used to verify grid convergence, as it contains results on the three grids used in this work. In the interior of the lid the pressure and stress converge with grid refinement, and the rate of convergence is that expected of a 2nd order method. However, grid refinement causes the pressure and stress to tend to infinity at the lid corners. This is because of the discontinuity which exists at these corners: the velocity jumps from zero (side walls) to one (lid). Due to this singularity, it was observed that the pressure and stress integrals over the lid do not converge with grid refinement, and so the shear force needed to drive the lid cannot be calculated accurately. The results on grid convergence are discussed later on. The increase in pressure with the Bingham number can also be seen in the pressure contours of Fig. 6. It is clear that the presence of the unyielded regions causes a distortion in the pressure field. The streamwise pressure gradients are greater inside the upper unyielded region.

An important issue when using the Papanastasiou regularisation is the choice of the exponent M. The higher the value of M, the better the approximation, but also the more difficult it is to solve the equations due to the increased degree of nonlinearity. Therefore, for practical reasons M has to be kept within certain limits. Here we provide some comparisons showing the effect of M on the quality of the results, while the issue of the computational effort required as a function of M will be investigated in the next section. One result of importance in a range of applications is the location of the yield lines, which are approximated in the present method by $\tau = Bn$, as previously stated. Fig. 7 shows that the use of the different values of 100, 200 and 400 for M does not affect the location of the yield lines significantly. The difference is especially small between $M = 400$ and $M = 200$. Fig. 8 shows iso-stress lines which deviate slightly from the yield stress value. Comparing Figs. 7 and 8 shows that the lines $\tau = \tau_y + \epsilon$ ($\epsilon > 0$) are less sensitive to the choice of M than the lines $\tau = Bn$. This verifies the result of Alexandrou and co-workers [33,40] that the location of iso-stress lines $\tau = \tau_y + \epsilon$ ($\epsilon > 0$) is predicted almost equally well for a range of M values, whereas to accurately predict the location of the yield line $\tau = \tau_y$ a high value of M is required. The iso-stress lines $\tau = \tau_y - \epsilon$ ($\epsilon > 0$) nearly coincide with the yield stress line except

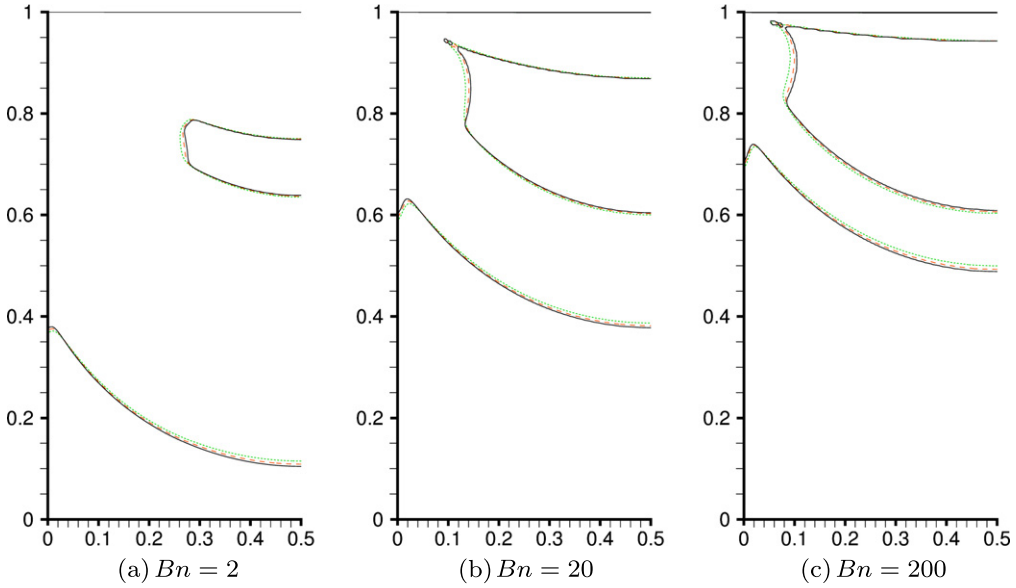

Fig. 7. Yield lines ($\tau = Bn$) calculated with $M = 100$ (dotted), $M = 200$ (dashed) and $M = 400$ (solid).

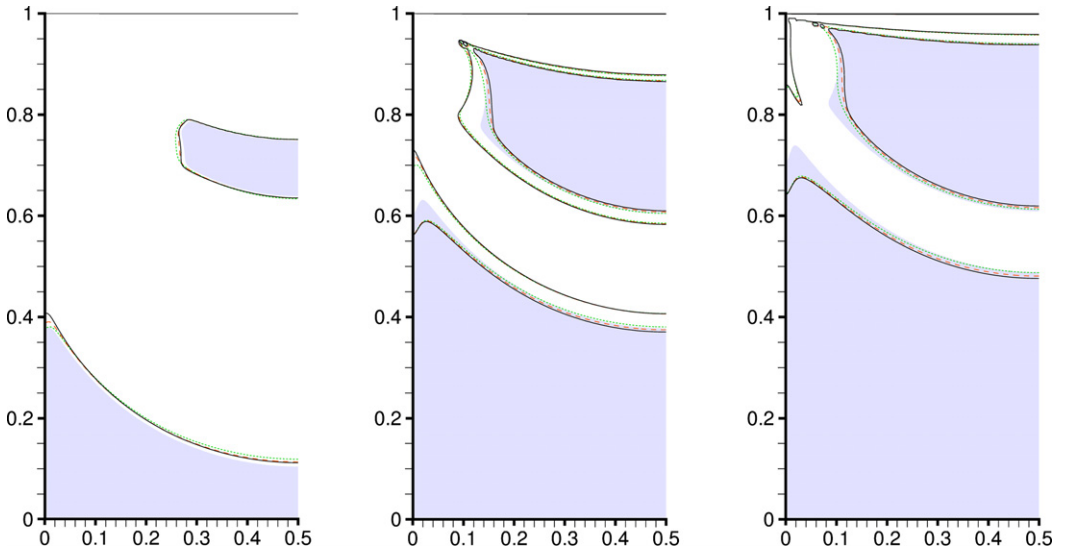

Fig. 8. Iso-stress lines calculated with $M = 100$ (dotted), $M = 200$ (dashed) and $M = 400$ (solid). Unyielded regions ($\tau \leqslant Bn$), calculated with $M = 400$, are shown shaded.

near the side walls and the lower corners of the upper unyielded region. Therefore, there is a sharp decrease in stress as one moves into the unyielded zone. On the contrary, this is not observed with the $\tau = \tau_y + \epsilon$ lines which are located at a distance from the yield line, meaning that the stress increases more gradually as one moves into the yielded zone. It is interesting to note that for $Bn = 200$ the difference between the actual stress and the yield stress is less than 1% throughout the fluid region that separates the two solid regions, since the $\tau = 1.01Bn$ contours do not cross into this region. So, the deformation rate is quite small there, and most of the shear takes place close to the lid.

In closing this section we provide some detailed results at the vertical centreline. The x velocity component (u) is plotted along the vertical centreline in Fig. 9. The limits of the yielded/unyielded zones can be clearly seen on that graph. On each curve (except for $Bn = 0$) two straight line segments can be identified. One is completely vertical with $u = 0$ and stretches from $y = 0$ up to a certain height; this segment corresponds to the lower unyielded zone which is motionless. The other segment corresponds to the upper unyielded zone; there the velocity is non-zero but decreases linearly with height, which shows that the upper unyielded zone rotates as a solid body. The centre of rotation can be estimated by extending the straight line segment until it intersects the $u = 0$ line.

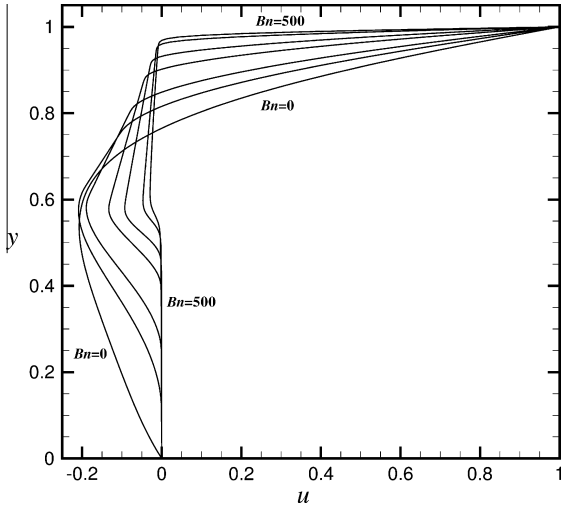

Fig. 9. The x component of velocity along the vertical centreline ($x = 0.5$), for $Bn = 0$, 2, 5, 20, 50, 200 and 500.

More detailed results are shown in Tables 1 ($Bn = 2$) and 2 ($Bn = 50$), where the velocity values have been obtained at selected points using linear interpolation from the values at adjacent CVs. To study grid convergence, results of various grids are also included. The exponent given in the tables is the order of grid convergence, which should be $q = 2$ for our present second-order accurate scheme. It is calculated by the following formula (see [34]):

$$q = \frac{\log\left(\frac{u_{128} - u_{64}}{u_{256} - u_{128}}\right)}{\log(2)} \tag{31}$$

where the subscripts denote the grid where u has been calculated.

Tables 1 and 2 show that $q \approx 1.5$ for $Bn = 2$, and $q \approx 1$ for $Bn = 50$. So, second-order convergence is not exhibited, which could be a sign that an even finer grid would be useful. However, the discretisation error is already relatively small as can be seen from the difference between the solutions at various grids. Besides, the use of a finer grid would significantly increase the computational cost as will be described in the next section. For $Bn = 50$ the value of q is especially low at the upper parts of the centreline, which is an indication that at higher Bn numbers (when most of the flow occurs at the upper part of the domain) it would be of benefit to use non-uniform grids with increased resolution near the top, or adaptive grids.

The last three columns of the tables are defined as follows:

$$\delta_{256}^{128} = 100 \cdot \left|\frac{u_{256}^{400} - u_{128}^{400}}{u_{256}^{400}}\right|\%, \quad \delta_{400}^{200} = 100 \cdot \left|\frac{u_{256}^{400} - u_{256}^{200}}{u_{256}^{400}}\right|\%,$$
$$\delta_{400}^{100} = 100 \cdot \left|\frac{u_{256}^{400} - u_{256}^{100}}{u_{256}^{400}}\right|\% \tag{32}$$

where u_n^m has been calculated on grid $n \times n$ with $M = m$. These values must be interpreted with caution, as they may appear large if u_{256}^{400} is close to zero. δ_{256}^{128} is a measure of the discretisation error, and it can be noticed that for $Bn = 2$ it is quite small, of the order

Table 1
Values of the x-component of velocity along the vertical centreline for $Bn = 2$.

Grid y	64×64 $M = 400$	128×128 $M = 400$	256×256 $M = 400$	256×256 $M = 200$	256×256 $M = 100$	q	δ^{128}_{256} (%)	δ^{200}_{400} (%)	δ^{100}_{400} (%)
1.00	1.00000	1.00000	1.00000	1.00000	1.00000	–	0.00	0.00	0.00
0.975	0.81421	0.81544	0.81581	0.81581	0.81581	1.74	0.05	0.00	0.00
0.950	0.63974	0.64222	0.64279	0.64280	0.64282	2.13	0.09	0.00	0.01
0.900	0.33677	0.34016	0.34121	0.34126	0.34136	1.69	0.31	0.02	0.04
0.850	0.10671	0.11033	0.11160	0.11172	0.11193	1.51	1.14	0.11	0.29
0.800	−0.04182	−0.03945	−0.03834	−0.03811	−0.03774	1.09	2.90	0.59	1.56
0.750	−0.10310	−0.10602	−0.10703	−0.10688	−0.10653	1.53	0.95	0.14	0.47
0.700	−0.13840	−0.14159	−0.14267	−0.14260	−0.14242	1.56	0.76	0.05	0.18
0.650	−0.17334	−0.17689	−0.17810	−0.17793	−0.17757	1.56	0.68	0.09	0.29
0.600	−0.20322	−0.20575	−0.20606	−0.20574	−0.20516	3.05	0.15	0.16	0.44
0.550	−0.20660	−0.20681	−0.20679	−0.20654	−0.20610	–	0.01	0.12	0.34
0.500	−0.18918	−0.18905	−0.18898	−0.18878	−0.18841	0.82	0.04	0.11	0.30
0.450	−0.16059	−0.16039	−0.16033	−0.16018	−0.15990	1.89	0.03	0.09	0.27
0.400	−0.12699	−0.12678	−0.12674	−0.12665	−0.12647	2.45	0.03	0.07	0.21
0.350	−0.09272	−0.09260	−0.09261	−0.09259	−0.09255	–	0.02	0.03	0.08
0.300	−0.06101	−0.06112	−0.06120	−0.06126	−0.06138	0.23	0.14	0.10	0.28
0.250	−0.03421	−0.03464	−0.03485	−0.03502	−0.03534	1.07	0.59	0.48	1.40
0.200	−0.01443	−0.01493	−0.01523	−0.01554	−0.01613	0.78	1.92	2.05	5.94
0.150	−0.00365	−0.00344	−0.00356	−0.00408	−0.00508	–	3.21	14.68	42.93
0.100	−0.00078	−0.00063	−0.00058	−0.00111	−0.00208	1.76	7.88	90.21	257.00
0.050	−0.00030	−0.00028	−0.00027	−0.00053	−0.00101	1.64	2.42	94.50	272.53
0.000	0.00000	0.00000	0.00000	0.00000	0.00000	–	0.00	0.00	0.00

Table 2
Values of the x-component of velocity along the vertical centreline for $Bn = 50$.

grid y	64×64 $M = 400$	128×128 $M = 400$	256×256 $M = 400$	256×256 $M = 200$	256×256 $M = 100$	q	δ^{128}_{256} (%)	δ^{200}_{400} (%)	δ^{100}_{400} (%)
1.0000	1.00000	1.00000	1.00000	1.00000	1.00000	–	0.00	0.00	0.00
0.9875	0.71205	0.72144	0.72838	0.72886	0.72931	0.43	0.95	0.07	0.13
0.9750	0.45957	0.47518	0.49123	0.49225	0.49324	−0.04	3.27	0.21	0.41
0.9500	0.10907	0.11660	0.13617	0.13835	0.14067	−1.38	14.38	1.60	3.30
0.9250	−0.01230	−0.01713	−0.01946	−0.01812	−0.01641	1.05	11.97	6.90	15.70
0.9000	−0.02462	−0.02952	−0.03123	−0.03106	−0.03073	1.52	5.49	0.56	1.60
0.8500	−0.03500	−0.03941	−0.04142	−0.04143	−0.04142	1.14	4.84	0.03	0.01
0.8000	−0.04469	−0.04914	−0.05148	−0.05156	−0.05165	0.93	4.55	0.16	0.33
0.7500	−0.05431	−0.05880	−0.06148	−0.06157	−0.06162	0.75	4.36	0.14	0.23
0.7000	−0.06386	−0.06840	−0.07142	−0.07145	−0.07135	0.59	4.23	0.04	0.09
0.6500	−0.07328	−0.07788	−0.08125	−0.08113	−0.08069	0.45	4.15	0.15	0.69
0.6000	−0.08172	−0.08678	−0.09080	−0.09033	−0.08917	0.33	4.43	0.52	1.80
0.5750	−0.08318	−0.08778	−0.09275	−0.09180	−0.08990	−0.11	5.36	1.03	3.08
0.5500	−0.07734	−0.07753	−0.08027	−0.07921	−0.07706	−3.91	3.42	1.32	3.99
0.5250	−0.06148	−0.05345	−0.05286	−0.05252	−0.05126	3.76	1.12	0.63	3.01
0.5000	−0.03959	−0.02641	−0.02406	−0.02464	−0.02484	2.49	9.75	2.41	3.23
0.4500	−0.00874	−0.00255	−0.00137	−0.00233	−0.00408	2.38	86.69	70.45	198.24
0.4000	−0.00153	−0.00076	−0.00069	−0.00135	−0.00263	3.46	10.19	96.74	283.34
0.3000	−0.00048	−0.00040	−0.00038	−0.00075	−0.00146	1.95	5.70	97.59	287.10
0.2000	−0.00026	−0.00022	−0.00021	−0.00042	−0.00083	1.99	4.82	97.74	287.60
0.1000	−0.00013	−0.00011	−0.00010	−0.00020	−0.00040	2.08	4.40	97.74	287.34
0.0000	0.00000	0.00000	0.00000	0.00000	0.00000	–	0.00	0.00	0.00

of 0.1–1%, whereas for $Bn = 50$ it is markedly larger, of the order of 5%. For $Bn = 2$, δ^{200}_{400} is of the order of 0.1%, while δ^{100}_{400} is about 3 times higher at each point. δ^{200}_{400} shows greater variability for $Bn = 50$, and is a little higher than for $Bn = 2$. δ^{100}_{400}, for $Bn = 50$, has about twice the value of δ^{200}_{400} in the upper part of the centreline, and three times the value of δ^{200}_{400} in the lower part. In general, it appears that, with the present choices of grid density and M, grid coarseness is a larger source of error than the smallness of M.

5. Convergence of the algebraic solver

When using the SIMPLE algorithm to solve Bingham flows, either as a single-grid solver or in a multigrid context, one realises that there is a severe deterioration of the convergence rates as the Bingham number increases. In Fig. 10 we plot against the number of iterations the L^∞-norm of the residual vector of the $x-$momentum equations,

$$\|r\|_\infty = \max_{P=1,\ldots,N}\{|r_P|\} \tag{33}$$

where r_P is the residual, expressed per unit volume, of the x-momentum equation of control volume P and N is the total number of control volumes in the grid. The residual norm is scaled by 1000 because in the actual numerical experiments we solved the dimensional version of the equations, with $L = 1$ m, $U = 1$ m/s, and $\mu = 1000$ Pa s. Therefore, the residuals of the dimensional equations are 1000 times larger than those of the dimensionless equations.

Fig. 10 shows that the performance of SIMPLE, as a single-grid solver, deteriorates as either Bn or M increases. The choices $a_u = 0.7$ and $a_p = 0.3$, used to obtain these results, are reasonable for Newtonian flows [34]. In Fig. 11, the effect of varying a_p is illus-

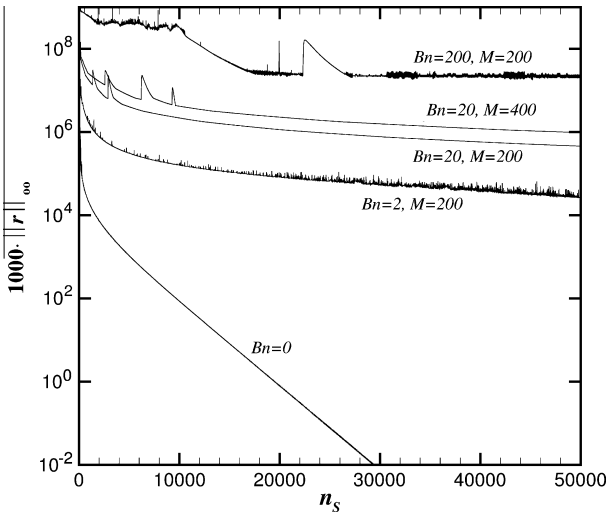

Fig. 10. The L^∞ norm of the x-momentum residual plotted against the number n_S of SIMPLE iterations, for single grid solution; $a_u = 0.7$, $a_p = 0.3$,256 × 256 grid.

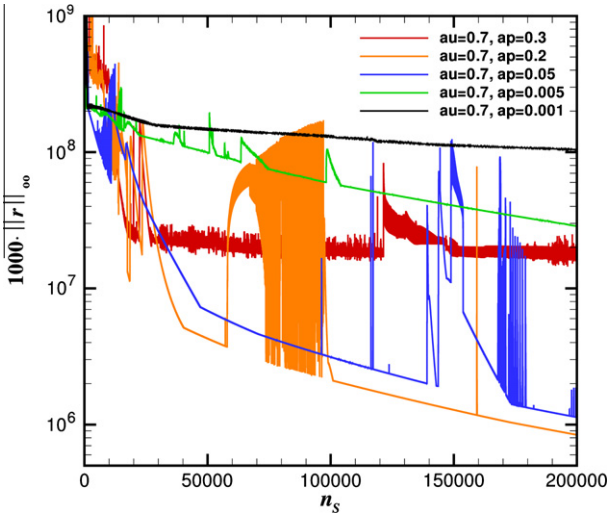

Fig. 11. The L^∞ norm of the x-momentum residual plotted against the number n_S of SIMPLE iterations, for single grid solution; $Bn = 200$, $M = 200$, 256 × 256 grid.

trated. As a_p is increased, convergence becomes faster, especially at the initial stages of iteration; however, it also becomes more oscillatory with large spikes. Beyond a certain value of a_p ($a_p = 0.3$ in Fig. 11) convergence stalls. On the other hand, using a very small a_p results in smooth but slow convergence. Due to the very large number of combinations of Bn, M, a_u, a_p and grid density, it is impossible to investigate fully the effect of all these parameters. We have observed (results not shown) that the performance of SIMPLE is similar also for other values of a_u in the range 0.8–0.2, but beyond these values it is difficult to obtain convergence.

The performance of SIMPLE as a smoother in a multigrid context is tested next. In applying multigrid, the coarsest grid used in the cycles was the 8 × 8 grid. According to our numerical experiments, the convergence deterioration of the SIMPLE algorithm with increasing Bn number also reflects on the multigrid performance. In fact, as Fig. 12 shows (solid lines), the multigrid method does not converge beyond a relatively small value of Bn, around 0.5. As a remedy, we applied the suggestion of Ferziger and Peric [34], that if a fluid property, such as the viscosity when RANS turbulence models are used, varies by orders of magnitude within the

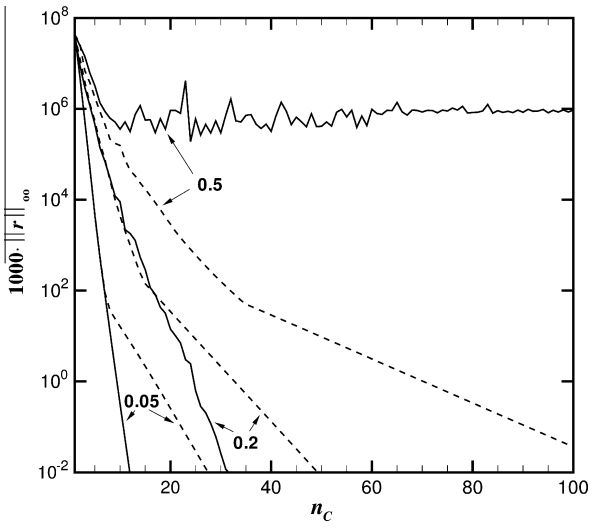

Fig. 12. The L^∞ norm of the x-momentum residual plotted against the number of multigrid cycles n_C, for $Bn = 0.05$, 0.2, and 0.5 ($M = 400$, grid 256 × 256). Solid lines depict convergence of the standard multigrid method, while dashed lines depict convergence of the modified multigrid method where viscosity is not updated at the coarse grids, but interpolated from the immediately finer grid.

computational domain, then it may be useful to update that property only on the finest grid and keep it constant within a multigrid cycle. So, we tried an implementation where the viscosity at coarse grids is not calculated afresh from (12) according to the restricted velocity field, but it is directly restricted (interpolated) from the immediately finer grid. The convergence of this modified multigrid method is also shown in Fig. 12 (dashed lines). The method converges more slowly than the standard multigrid method, but it is more robust and can converge over a wider range of Bingham numbers. Both methods converge equally fast up to a point, beyond which the convergence of the modified method suddenly slows down. It appears that both methods are equally capable of reducing certain components of the residual, which dominate the residual at the initial stages of iteration. However, the modified method is less capable of reducing certain other components, which dominate the error beyond a certain point.

The modified method is not strictly "multigrid" since part of the solution, namely the updating of the viscosity, only takes place on the finest grid. Therefore the method exhibits also some single-grid convergence characteristics. In particular, as Fig. 13 shows for $Bn = 0.05$, the convergence of the modified method slows down as the grid is refined (this is true only for those slowly converging components of the residual). On the contrary, the standard method converges equally fast on all grids, which is normal multigrid behaviour.

For higher Bingham numbers it is necessary to use the modified multigrid method, and even in that case convergence difficulties are encountered. However, the gains compared to the single-grid method are still quite impressive. Fig. 14 shows the convergence rates for various Bingham numbers, using both single-grid (SG) and multigrid (MG) procedures. In each case the solution on the 128 × 128 grid was used as the initial guess and the coarsest grid used by the multigrid cycles was the 8 × 8 grid. The computational effort (x-axis) is measured in terms of equivalent fine-grid SIMPLE iterations. For the single-grid cases, this is just the number of SIMPLE iterations performed. For the multigrid cases, the number of cycles is multiplied by the number of fine-grid SIMPLE iterations that cost computationally the same as a single cycle. For example, n_C W(ν_1, ν_2) − ν_3 cycles cost approximately the same as $n_S = n_C \cdot [2(\nu_1 + \nu_2) + \nu_3]$ SIMPLE iterations on the finest grid, as mentioned in Section 3.2. It should be noted that the cost of

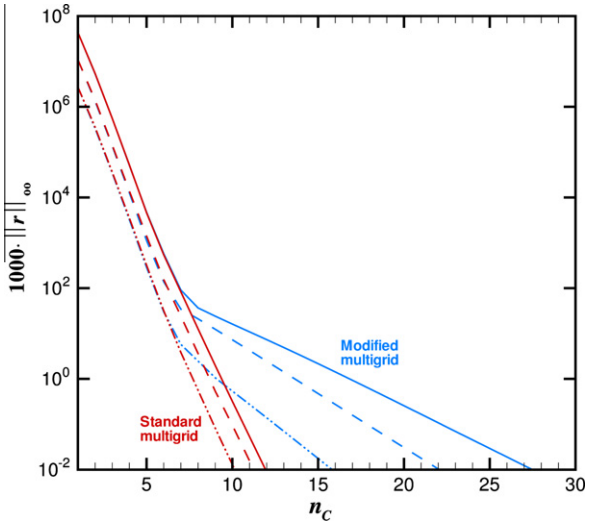

Fig. 13. The L^∞ norm of the x-momentum residual plotted against the number of multigrid cycles, n_C, for $Bn = 0.05$, $M = 400$, on various grids: 64×64 (chained lines), 128×128 (dashed lines), and 256×256 (solid lines). In the modified multigrid method, viscosity is not updated at the coarse grids, but simply interpolated from the immediately finer grid.

restriction and prolongation is omitted in this calculation, since the cost of these operations is very small compared to the cost of the SIMPLE iterations, especially if one considers that the numbers of pre-and post-smoothing iterations are large, and fine-grid iterations are also carried out between cycles. Therefore, MG and SG convergence rates are directly comparable in Fig. 14.

One may also observe that as the Bn number increases, the choice of multigrid parameters becomes rather unusual compared to the usual multigrid practice: the number of pre-and post-smoothing sweeps is quite large, and a large number of SIMPLE iterations are required between cycles. These choices of parameters have been found necessary to obtain convergence. It may also be seen that very small values of a_p were used in the multigrid cases. This was necessary, otherwise the procedure did not converge. This may be associated with the fact that, as a_p increases, SIMPLE converges faster but in a very oscillatory manner, which may cause problems to the multigrid procedure. Since the single-grid procedure converges faster when a_p is as large as possible, the SG results have been obtained with large values of a_p, compared with the MG cases. It can be observed that multigrid is extremely efficient at low Bn numbers, but has difficulty when Bn is large. Yet, in every case the multigrid convergence rates are much faster than the single-grid rates, except for the first few iterations. Therefore multigrid is preferable in any case. Moreover, we note that multigrid (with the particular choices of parameters) converges faster for $Bn = 200$ with $M = 200$ than for $Bn = 20$ with $M = 400$. Indeed we observed in every case that convergence deteriorates significantly not only with increasing Bn but also with increasing M (for every Bingham number we solved the problem using $M = 100$, 200, and 400, except for $Bn = 500$ and 1000 where only $M = 100$ was used due to convergence difficulties).

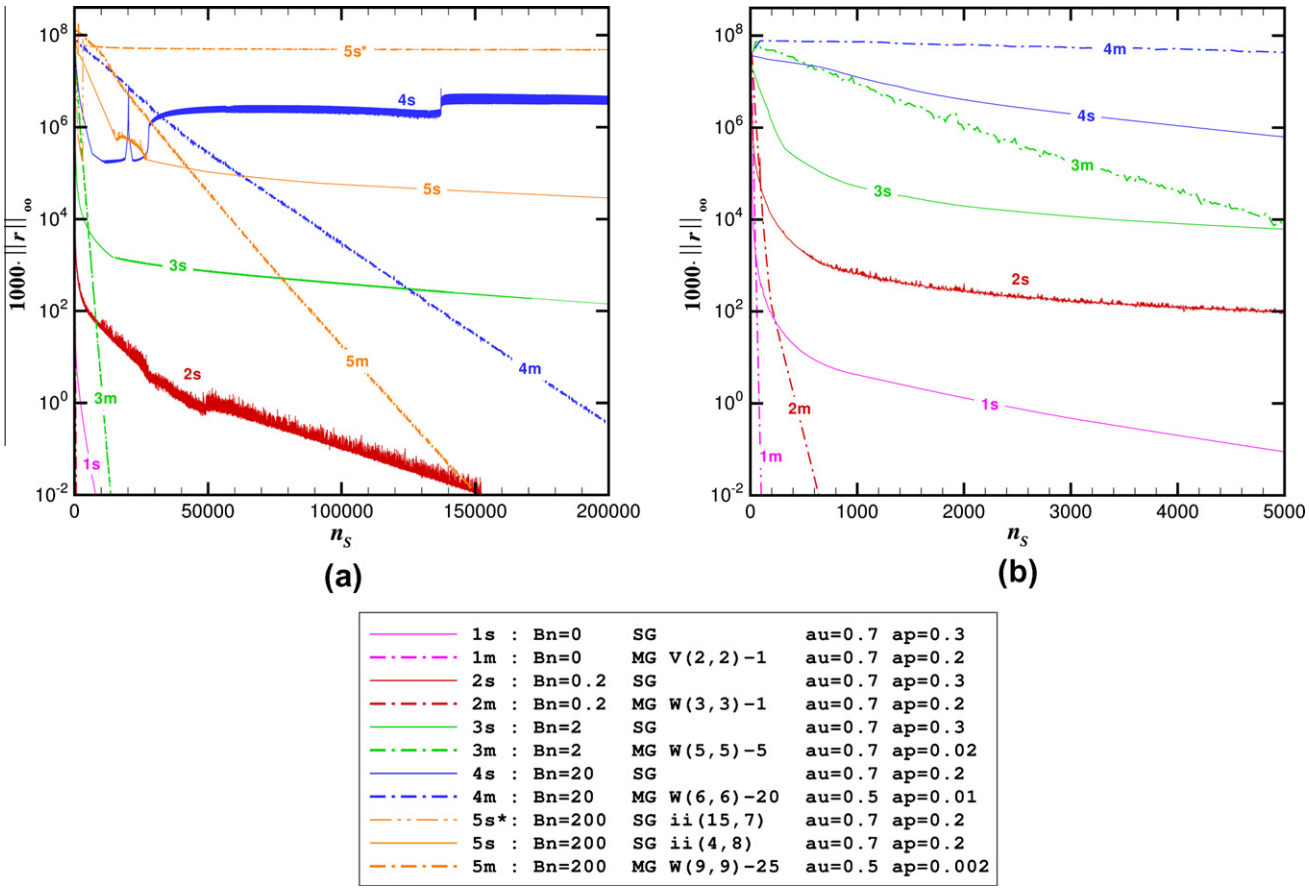

Fig. 14. (a) The L^∞ norm of the x-momentum residual on the 256×256 grid plotted against the number of equivalent fine-grid SIMPLE iterations, n_S. In all cases $M = 400$, except $M = 200$ for $Bn = 200$. SG and MG denote respectively single-grid and multigrid solution procedures, the initial guess being the solution of the immediately finer (128×128) grid. (b) Zoom-in of (a) so that the curves `1m` and `2m` (which are too close to the vertical axis to be visible in (a)) are visible. Also, to improve the readability, the results for $Bn = 200$ have been omitted from graph (b).

It is worth mentioning that the number of inner iterations seems to play an important role. In Fig. 14 it can be seen that for $Bn = 200$, using 4 GMRES iterations and 8 CG iterations for the velocity and pressure correction systems (labelled "ii(4,8)" in the figure) significantly improves the convergence rate of the single-grid procedure compared to the case that 15 and 7 iterations are used instead (labelled "ii(15,7)"). It seems that due to the nonlinearity of the algebraic system it is better not to perform many iterations on the linearised velocity systems within each SIMPLE outer iteration. This was not investigated in detail, due to the fact that there are already a large number of parameters involved in the solution procedure.

6. Conclusions

We have solved the creeping lid-driven cavity flow of a Bingham plastic using the Papanastasiou regularisation and the finite volume method combined with a multigrid algorithm. Results have been obtained for Bingham numbers in the range 0–1000. These compare favourably with the results of other methods, such as the finite-element and the finite-difference method, and show that the proposed method provides a useful tool in solving viscoplastic flows for a wide range of Bingham numbers. It should be noted that the convergence of the method becomes slow at high values of the Bingham number and the regularisation parameter. With the use of a modified multigrid method convergence is accelerated considerably compared to the single-grid SIMPLE method.

Acknowledgements

This work was co-funded by the European Regional Development fund and the Republic of Cyprus through the Research Promotion Foundation (research project ΑΕΙΦΟΡΙΑ/ΦΥΣΗ/0609(BIE)/15).

References

[1] H.A. Barnes, The yield stress – a review or '$\pi\alpha\nu\tau\alpha\ \rho\epsilon\iota$' – everything flows?, J Non-Newton. Fluid Mech. 81 (1999) 133–178.
[2] E.C. Bingham, Fluidity and Plasticity, McGraw-Hill, New York, 1922.
[3] T.C. Papanastasiou, Flows of materials with yield, J. Rheol. 31 (1987) 385–404.
[4] I. Frigaard, C. Nouar, On the usage of viscosity regularisation methods for visco-plastic fluid flow computation, J. Non-Newton. Fluid Mech. 127 (2005) 1–26.
[5] E. O'Donovan, R. Tanner, Numerical study of the Bingham squeeze film problem, J. Non-Newton. Fluid Mech. 15 (1984) 75–83.
[6] M. Fortin, R. Glowinski, Augmented Lagrangian Methods: Applications to the Numerical Solution of Boundary-Value Problems, North-Holland, Amsterdam, 1983.
[7] R. Glowinski, Numerical Methods for Nonlinear Variational Problems, Springer, New York, 1984.
[8] E.J. Dean, R. Glowinski, G. Guidoboni, On the numerical simulation of Bingham visco-plastic flow: old and new results, J. Non-Newton. Fluid Mech. 142 (2007) 36–62.
[9] P. Neofytou, A 3rd order upwind finite volume method for generalised Newtonian fluid flows, Adv. Eng. Softw. 36 (2005) 664–680.
[10] S.V. Patankar, D.B. Spalding, A calculation procedure for heat, mass and momentum transfer in three-dimensional parabolic flows, Int. J. Heat Mass Transfer 15 (1972) 1787–1806.
[11] O. Turan, N. Chakraborty, R.J. Poole, Laminar natural convection of Bingham fluids in a square enclosure with differentially heated side walls, J. Non-Newton. Fluid Mech. 165 (2010) 901–913.
[12] O. Turan, N. Chakraborty, R.J. Poole, Laminar Rayleigh-Benard convection of yield stress fluids in a square enclosure, J. Non-Newton. Fluid Mech. 171–172 (2012) 83–96.
[13] P. Neofytou, D. Drikakis, Effects of blood models on flows through a stenosis, Int. J. Numer. Meth. Fluids 43 (2003) 597–635.
[14] P. Neofytou, D. Drikakis, Non-Newtonian flow instability in a channel with a sudden expansion, J. Non-Newton. Fluid Mech. 111 (2003) 127–150.
[15] P.R. de Souza Mendes, M.F. Naccache, P.R. Varges, F.H. Marchesini, Flow of viscoplastic liquids through axisymmetric expansions–contractions, J. Non-Newton. Fluid Mech. 142 (2007) 207–217.
[16] M.F. Naccache, R.S. Barbosa, Creeping flow of viscoplastic materials through a planar expansion followed by a contraction, Mech. Res. Commun. 34 (2007) 423–431.
[17] O. Botella, R. Peyret, Benchmark spectral results on the lid-driven cavity flow, Comput. Fluids 27 (1998) 421–433.
[18] A. Syrakos, A. Goulas, Finite volume adaptive solutions using SIMPLE as smoother, Int. J. Numer. Meth. Fluids 52 (2006) 1215–1245.
[19] C.-H. Bruneau, M. Saad, The 2D lid-driven cavity problem revisited, Comput. Fluids 35 (2006) 326–348.
[20] F. Sanchez, Application of a first-order operator splitting method to Bingham fluid flow simulation, Comput. Math. Appl. 36 (1998) 71–86.
[21] E. Mitsoulis, T. Zisis, Flow of Bingham plastics in a lid-driven square cavity, J. Non-Newton. Fluid Mech. 101 (2001) 173–180.
[22] D. Vola, L. Boscardin, J. Latch, Laminar unsteady flows of Bingham fluids: a numerical strategy and some benchmark results, J. Comput. Phys. 187 (2003) 441–456.
[23] R. Elias, M. Martins, A. Coutinho, Parallel edge-based solution of viscoplastic flows with the SUPG/PSPG formulation, Comput. Mech. 38 (2006) 365–381.
[24] Z. Yu, A. Wachs, A fictitious domain method for dynamic simulation of particle sedimentation in Bingham fluids, J. Non-Newton. Fluid Mech. 145 (2007) 78–91.
[25] M.A. Olshanskii, Analysis of semi-staggered finite-difference method with application to Bingham flows, Comput. Meth. Appl. Mech. Eng. 198 (2009) 975–985.
[26] J. Zhang, An augmented Lagrangian approach to Bingham fluid flows in a lid-driven square cavity with piecewise linear equal-order finite elements, Comput. Meth. Appl. Mech. Eng. 199 (2010) 3051–3057.
[27] D.D. dos Santos, S. Frey, M.F. Naccache, P. de Souza Mendes, Numerical approximations for flow of viscoplastic fluids in a lid-driven cavity, J. Non-Newton. Fluid Mech. 166 (2011) 667–679.
[28] R.P. Fedorenko, A relaxation method for solving elliptic difference equations, USSR Comput. Math. Math. Phys. 1 (1962) 1092–1096.
[29] A. Brandt, Multi-level adaptive solutions to boundary-value problems, Math. Comput. 31 (1977) 333–390.
[30] S. Sivaloganathan, G.J. Shaw, A multigrid method for recirculating flows, Int. J. Numer. Meth. Fluids 8 (1988) 417–440.
[31] M. Hortmann, M. Peric, G. Scheuerer, Finite volume multigrid prediction of laminar natural convection: benchmark solutions, Int. J. Numer. Meth. Fluids 11 (1990) 189–207.
[32] J.A. Tsamopoulos, M.E. Chen, A.V. Borkar, On the spin coating of viscoplastic fluids, Rheol. Acta 35 (1996) 597–615.
[33] G.R. Burgos, A.N. Alexandrou, V. Entov, On the determination of yield surfaces in Herschel–Bulkley fluids, J. Rheol. 43 (1999) 463–483.
[34] J.H. Ferziger, M. Peric, Computational Methods for Fluid Dynamics, third ed., Springer, 2002.
[35] A. Syrakos, A. Goulas, Estimate of the truncation error of finite volume discretization of the Navier–Stokes equations on colocated grids, Int. J. Numer. Meth. Fluids 50 (2006) 103–130.
[36] C.M. Rhie, W.L. Chow, Numerical study of the turbulent flow past an airfoil with trailing edge separation, AIAA J. 21 (1983) 1525–1532.
[37] S.V. Patankar, Numerical Heat Transfer and Fluid Flow, Hemisphere, 1980.
[38] Y. Saad, Iterative Methods for Sparse Linear Systems, second ed., SIAM, 2003.
[39] G.J. Shaw, S. Sivaloganathan, On the smoothing properties of the SIMPLE pressure-correction algorithm, Int. J. Numer. Meth. Fluids 8 (1988) 441–461.
[40] G.R. Burgos, A.N. Alexandrou, Flow development of Herschel–Bulkley fluids in a sudden three-dimensional square expansion, J. Rheol. 43 (1999) 485–498.